Korean J. Chem. Eng., 34(12), 3200-3207 (2017)
DOI: 10.1007/s11814-017-0222-y

pISSN: 0256-1115
eISSN: 1975-7220

Plasmon-enhanced ZnO nanorod/Au NPs/Cu_2O structure solar cells: Effects and limitations

Il-Han Yoo*, Shankara Sharanappa Kalanur*, Kiryung Eom*, Byungmin Ahn*, In Sun Cho*, Hak Ki Yu*, Hyeongtag Jeon,†, and Hyungtak Seo*,†**

*Department of Energy Systems Research and Department of Materials Science & Engineering, Ajou University, Suwon 16499, Korea
**Division of Materials Science & Engineering, Hanyang University, Seoul 04763, Korea
(*Received 23 May 2017 • accepted 9 August 2017*)

Abstract−Cu-based compounds can be a good candidate for a low cost solar cell material. In particular, Cu_xO (x : 1-2) has a good visible light absorbing bandgap at 1-2 eV. As for using nanostructures in solar cell applications, metal nanoparticle-induced localized plasmon resonance is a promising way to increase light absorbance, which can help improve the efficiency of solar cells. We fabricated ZnO nanorod/Au nanoparticles/Cu_2O nanostructures to study their solar cell performance. ZnO nanorods and Cu_2O layer were synthesized by the electrodeposition method. Size-controlled Au nanoparticles were deposited using E-beam evaporator for localized surface plasmon resonance (LSPR) effect. By inserting Au plasmon nanoparticles and annealing Au NPs in solar cells, we could tune the maximum incident photon-to-current efficiency wavelength. However, the potential well formed by Au NP at the ZnO/Cu_2O junction leads to charge-trapping, based on the constructed electronic band analysis. LSPR-induced hot carrier generation is proposed to promote carrier transport further in the presence of Au NPs.

Keywords: Au Plasmon Nanoparticle, LSPR, ZnO/Cu_2O Solar Cells, Oxide Solar Cells, Electronic Band Analysis

INTRODUCTION

Since solar cells are one of most important renewable energy technologies, using the sun as the unlimited and eco-friendly light source [1], there has been tremendous research to commercialize various emerging types of solar cells, such as perovskite, organic, quantum dot and thin film solar cells. However, at present, the solar cells mainly used in the industry are Si-based solar cells, which have high production cost, in spite of many recent efforts to reduce the manufacturing cost. A major issue in Si solar cells is having to use expensive single-crystalline Si wafer for the high-efficiency cell, while achieving only low efficiency with the low-cost manufacturing process using amorphous or polycrystalline silicon. This necessitates seeking other effective solar cell materials with a lower cost, but higher efficiency. Among the various solar cell materials that can replace Si-based solar cells, metal oxide solar cells show promise. Copper oxide is a potential metal oxide solar cell material, since it is p-type with narrow bandgaps at 1.1-2.5 eV, in addition to being earth-abundant and nontoxic [2-4]. Furthermore, it has a high absorption coefficient in the visible range that is effective for solar cells [5,6]. ZnO is the most successful n-type counterpart material to copper oxide, because of its band edge structures. Moreover, ZnO has a wide band gap, due to which it can be used for window layers [7,8]. Nevertheless, oxide hybrid solar cells (HSC) have been consistently reported to have low efficiency, due to poor minority carrier diffusion length for adequate optical absorption [9-11]. In this study, in order to overcome this limitation of low efficiency oxide HSC, we applied localized surface plasmon resonance (LSPR) to nanostructured ZnO/Cu_2O HSC. Compared to the conventional planar interface structure, nanostructures have shown increased interfaces where photo-generated carriers are separated, thereby resulting in improved solar cell performance [12-14]. Moreover, LSPR is occasionally utilized for solar cell application to improve the light absorption efficiency. LSPR can be easily controlled by the metal type, size, and shape of the LSPR nanoparticles [15-17]. Due to these benefits, LSPR has recently been applied to many kinds of solar cells, such as organic solar cells, dye-sensitized solar cells, and perovskite solar cells [18-20]. In the previous literature, there were many works about ZnO nanorod and Cu_2O structure [21-27]. However, no research about adding Au nanoparticles for LSPR between the ZnO/Cu_2O nanohybrid structure was made as clarifying in a view of electronic band structure in addition to an effect of light absorption, which is a main application of LSPR. In this study, we fabricated ZnO nanorod nanostructures, completely covered with Cu_2O layer for the creation of a 3-dimensional interface. Secondly, in fixed structure and materials, Au nanoparticles (Au NPs) were inserted at ZnO/Cu_2O interface, to induce LSPR effect, in order to shift the photon harvesting wavelength to visible light range, which has higher energy in the solar spectrum [19,20,28].

EXPERIMENTAL

The ZnO nanorod and Cu_2O layer were prepared by electrodeposition methods, while gold was deposited using an E-beam evap-

†To whom correspondence should be addressed.
E-mail: hjeon@hanyang.ac.kr, hseo@ajou.ac.kr

orator for LSPR nanoparticles and top electrode. For electrodeposition, we used a conventional three-electrode system that uses platinum as a counter electrode and Ag/AgCl as the reference electrode, with an Ivium-n-Stat from Ivium technologies (Netherlands). ZnO nanorod was deposited on fluorine-doped tin oxide (FTO) glass substrate at −1.0 V for 45 min, using aqueous solutions of 5×10^{-4} M $ZnCl_2$ and 0.1 M KCl at 78 °C. The thickness of the ZnO nanorod was about 260 nm, and the length was 1 μm. On the ZnO nanorod, Au nanoparticles were deposited up to a thickness of 5 nm, subsequently being annealed using a furnace with air supply for 1 h at 200 and 250 °C. Cu_2O was electrodeposited at −1.0 mA/cm^2 for 33 min using aqueous solutions of 0.4 M $CuSO_4$ and 3 M lactic acid, with 4 M NaOH to adjust the pH to 12.5 at 40 °C. To prepare the solar cells and the diode structure, Au top electrodes were deposited onto Cu_2O at 100 nm thickness.

The ultraviolet-visible (UV-vis) absorption spectra and optical bandgaps were measured using an Avantes spectroscopy system with an AvaLight-DH-S-BAL balanced power source and AvaSpec-ULS2048 Starline versatile fiber-optic spectrometer detector (Netherlands). The morphology and size of Au nanoparticles were measured by transmission electron microscopy (TEM; FEI Tecnai G2 F30 S-Twin USA). X-ray diffraction (XRD) was measured using a Rigaku MiniFlex-II desktop X-ray diffractometer (Japan). The morphology and size of the nanostructures were measured by field emission scanning electron microscopy (FE-SEM; JEOL JSM-6700F Japan). Surface chemical binding states and valence band-edge states were measured by X-ray photoelectron spectroscopy (XPS; theta probe base system, Thermo Fisher Scientific Co. USA). IPCE analy-

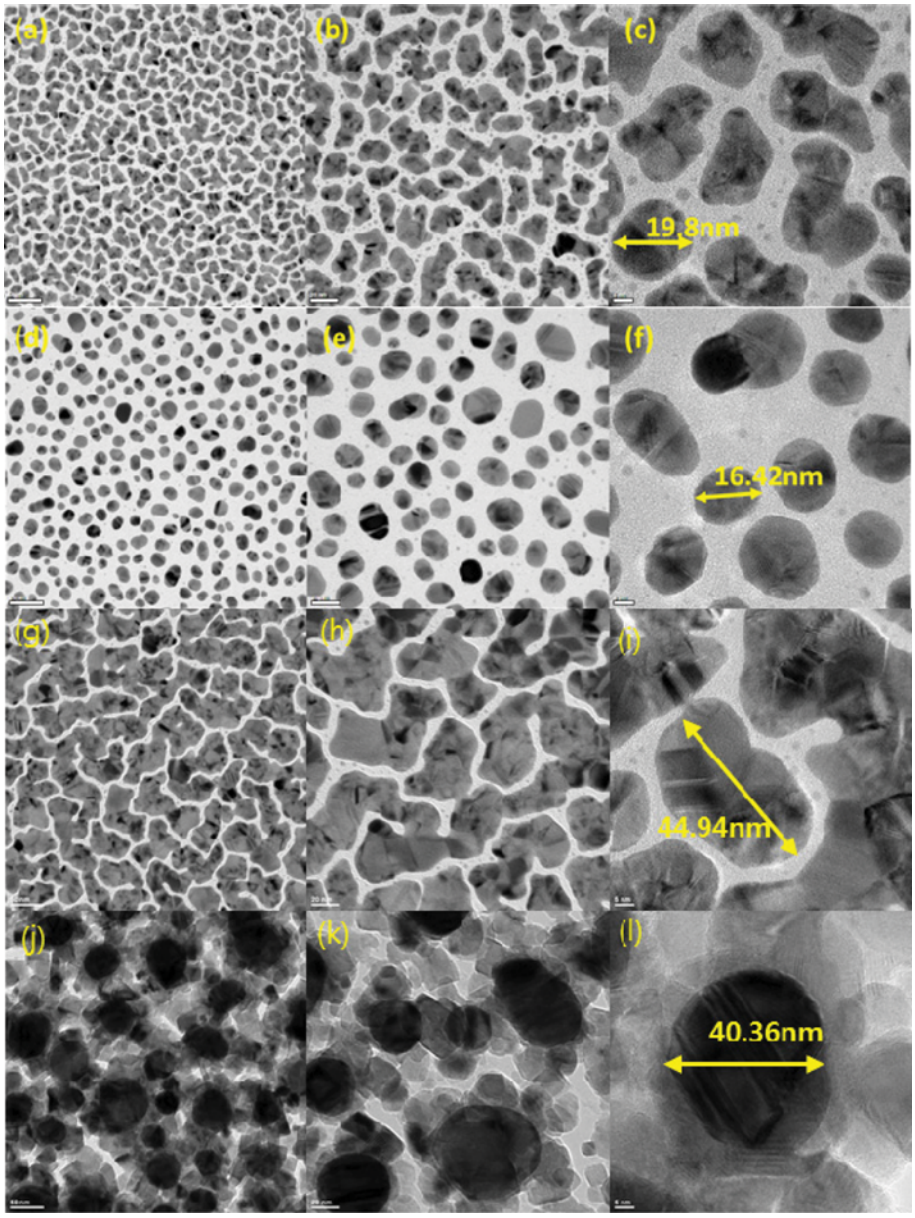

Fig. 1. TEM images of (a), (b), (c) 5-nm Au nanoparticles, (d), (e), (f) 5-nm Au nanoparticles with 200 °C annealing, (g), (h), (i) 10-nm Au nanoparticles, and (j), (k), (l) 10-nm Au nanoparticles with 200 °C annealing.

sis involved using an Ivium-n-Stat from Ivium technologies (Netherlands) and monochromatic light at 300-900 nm from a xenon lamp. An Optical power meter (Newport 1936-R USA) was used to calculate the IPCE.

RESULTS AND DISCUSSION

The localized surface plasmon effect is dependent on the particle size and shape. To find the most appropriate size and annealing condition of Au nanoparticles for localized surface plasmon effect in solar cell applications, we deposited gold nanoparticles on the glass substrate using an E-beam evaporator at 5 and 10 nm thickness, subsequently annealing each sample at 150, 200, and 250 °C for 1 hr. These Au NPs were evaluated by TEM (Fig. 1) and UV-vis optical absorbance (Fig. 2). TEM images indicate that the as-deposited Au NPs formed an island-like shape with irregular NP size distribution. However, after annealing Au NPs, the NPs took a spherical shape. Moreover, NP sizes were reduced and distribution became even with NP size. Comparing 5 and 10 nm thick Au NP, 5 nm thick Au NPs have even NP sizes at 15-20 nm, becoming smaller than the thick Au NP size at 40-50 nm after annealing. As the annealing temperature increased, Au NP sizes decreased [29-31]. UV-Vis absorbance spectra show that the as-deposited Au NPs absorbed a wide range of visible light at wavelength>500 nm. When annealing Au NPs, the absorbance displays the typical features of LSPR absorbance in Au NPs. As the annealing temperature increases, LSPR absorption band becomes narrow, and overall absorption peaks are blue shifted from 560 to 540 nm. This is because the shape of the Au nanoparticles changes from random to spherical, thereby causing the random scattering effect to decrease, while the coherent LSPR effect increases as the size decreases. Moreover, the visible color of the sample with Au NPs changes from sky blue to pink after annealing. Through these TEM and absorbance data that shows more LSPR effect at 5 nm thickness, the deposition of Au NPs was set to E-beam deposition at 5 nm thickness, with post E-beam deposition annealing.

To confirm the phase of electrodeposited (a) ZnO nanorod/Au NP structure and (b) ZnO nanorod/Au/Cu_2O oxide structure on FTO substrate, XRD measurements were carried out (Fig. 3). From Fig. 3(a), it can be confirmed that the ZnO nanorod developed satisfactorily, with good crystallinity (JCPDS-00-036-1451). From Fig. 3(b), it can be noted that the Cu_2O phase is predominant (JCPDS-00-100-0063), while the CuO sub-phase cannot be found. Neither of the XRD data revealed Au NPs, which are too thin for

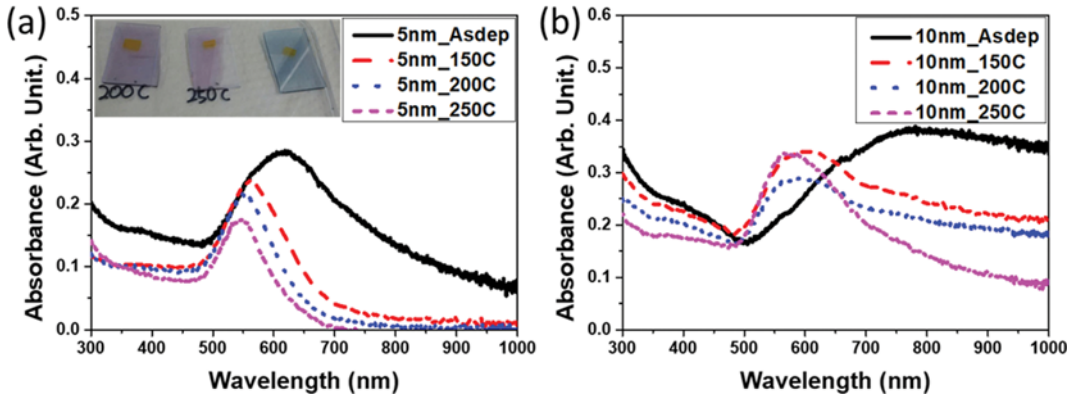

Fig. 2. UV-vis absorbance data for (a) 5-nm Au nanoparticles with 150, 200, 250 °C annealing and (b) 10-nm Au nanoparticles with 150, 200, 250 °C annealing.

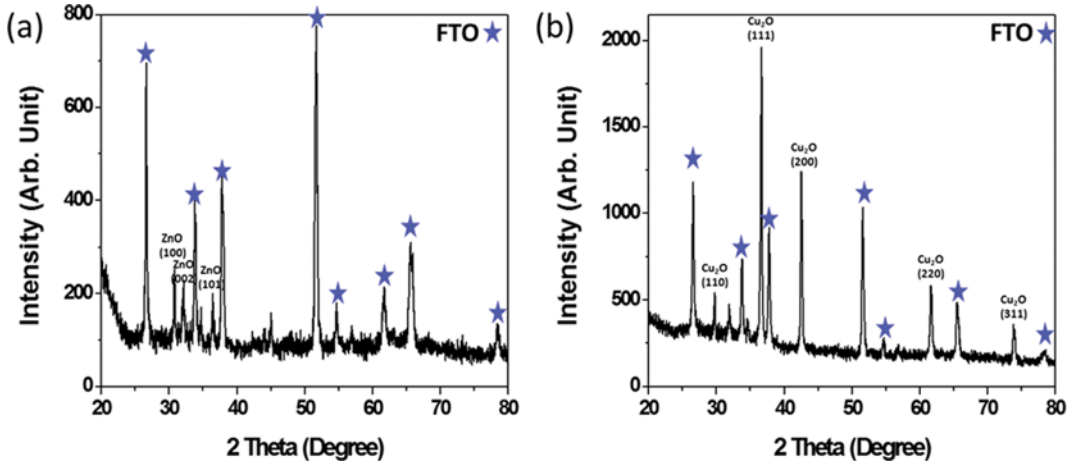

Fig. 3. XRD patterns of (a) ZnO nanorod/Au NP on FTO and (b) ZnO nanorod/Au NP/Cu_2O on FTO.

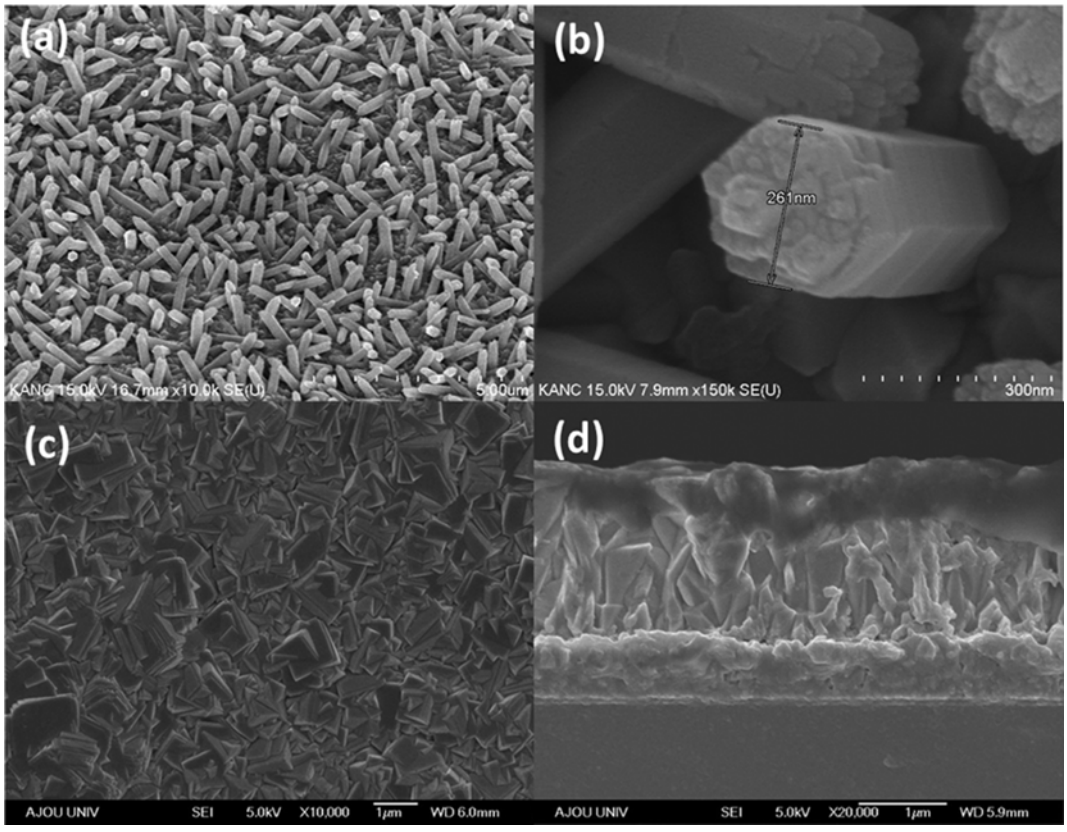

Fig. 4. SEM images of (a), (b) ZnO nanorod and (c), (d) ZnO nanorod/Cu_2O structure.

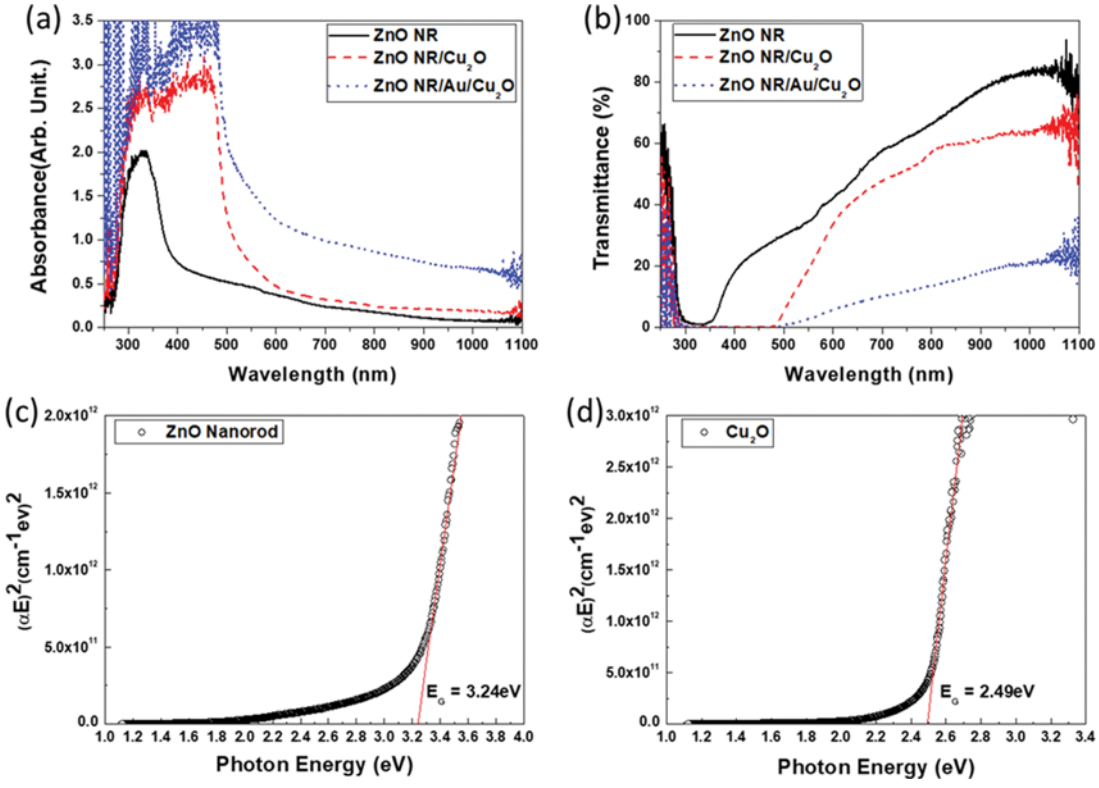

Fig. 5. UV-vis spectroscopy analyzed (a) absorbance and (b) transmittance of ZnO nanorod, ZnO nanorod/Cu_2O, ZnO nanorod/Au NP/Cu_2O. The extracted optical bandgap of (c) ZnO and (d) Cu_2O, from Tauc plots.

X-ray diffraction. The morphology of the electrodeposited ZnO nanorod and ZnO nanorod/Cu_2O structure was analyzed using SEM (Fig. 4). ZnO nanorod structure was well-developed, with a hexagonal structure. The diameter of the nanorod was approximately 260 nm. The SEM image of Cu_2O showed large crystal grains, a few μm in size (Fig. 4(c)). From the cross-sectional SEM image (Fig. 4(d)) of the ZnO/Cu_2O heterostructure, we could find that Cu_2O covered the ZnO nanorods completely from the bottom to top, without any gaps or holes.

To check the effect of Au NP induced LSPR on the optical absorbance in ZnO/Cu_2O nanostructured HSC, UV-Vis spectroscopic analysis was performed on the ZnO nanorod and the ZnO nanorod/Cu_2O structure, with and without Au NP insertion (Fig. 5). For this measurement, Cu_2O was deposited at a thickness of 740 nm, since 2.4 μm of deposited Cu_2O was too thick to be measured by UV-Vis spectroscopy due to its opaqueness. By adding Au plasmon NPs, the visible light absorption increased from 500 nm wavelength. From the optical transmittance data, the optical bandgap was extracted using the Tauc plot (Fig. 5). The Tauc plot ($\alpha h\nu^{1/n}$ vs. $h\nu$) curve was calculated with n=1/2 (in the case of direct bandgap) and α as the absorption coefficient [32,33]. From this, the optical band gaps of ZnO nanorod and Cu_2O were calculated to be 3.24 eV and 2.49 eV, respectively.

IV characteristics of the synthesized ZnO nanorod/Cu_2O nanostructure heterojunction were evaluated (Fig. 6). From I-V measurements, it was confirmed that nanostructure forms p-n junction with diode characteristics, which is essential for solar cells formation. The rectification factor, which is calculated by the ratio of reverse current (+bias polarity) to forward current (−bias polarity), ranges up to 30 at 5 V.

The normalized incident photon-to-current efficiency (IPCE) confirmed the effect of Au LSPR nanoparticles on the solar efficiency (Fig. 7). In ZnO nanorod/Cu_2O structure without Au NPs, the maximum IPCE appeared in the 400 nm region. Interestingly, after the deposition of Au, ZnO nanorod/Cu_2O showed red shift the IPCE curve. Furthermore, the maximum IPCE peak shift from 400 to 500 nm was observed for samples containing 5 nm Au NP annealed at 250 °C. (The width of the ZnO nanorod was about 260 nm, and the length was 1 μm). From this, we could adjust the wavelength in the IPCE of solar cells by adding Au nanoparticle

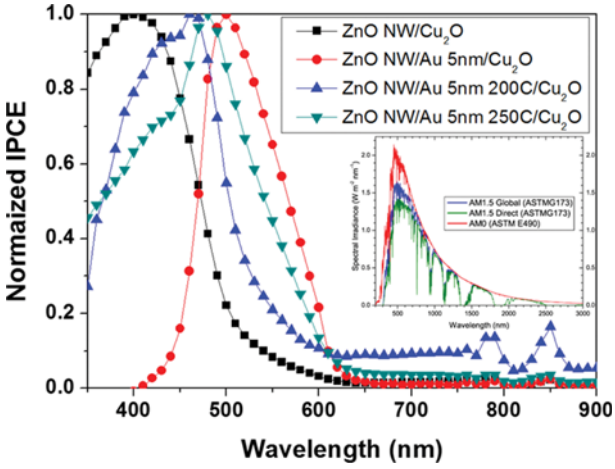

Fig. 7. IPCE of ZnO nanorod/Cu_2O, ZnO nanorod/Au NP/Cu_2O, ZnO nanorod/Au NP Au 5-nm (200 °C anneal)/Cu_2O and ZnO nanorod/Au 5-nm (250 °C anneal)/Cu_2O samples.

and annealing. This suggests that it is possible to match the wavelength of IPCE peak with reference to the solar spectrum (Fig. 7 inset) [34], thereby increasing the efficiency of oxide solar cells of a given structure and materials.

XPS spectroscopy of ZnO nanorod/Cu_2O heterostructure was used to investigate the band electronic structures of heterostructures (Fig. 8) and the effect of Au insertion (Fig. 9). For this measurement, Cu_2O was deposited on ZnO nanorod at a thickness of 6 nm, with only a 5-s E-beam deposition to measure the physicochemical characteristics at the interface. From the XPS survey spectra of the interface region, we found strong-intensity Zn 2p peak and weak-intensity Cu 2p peak, which means that ZnO nanorod and the top layer of Cu_2O coexist within the photoelectron escape depth. To construct the heterojunction band alignment model, valence band maximum (VBM) was extracted by the extrapolation of VB edge onset. Fig. 8(a) shows the VBM of ZnO nanorod and Cu_2O as 2.2 eV and 0.2 eV, respectively. Then, the valence band offset (VBO) and conduction band offset (CBO) of the ZnO nanorod/Cu_2O were calculated along with the acquired optical bandgaps, VBM data and XPS-extracted core level shifts at the interface of each set of materials, using the theory of Kraut as shown in

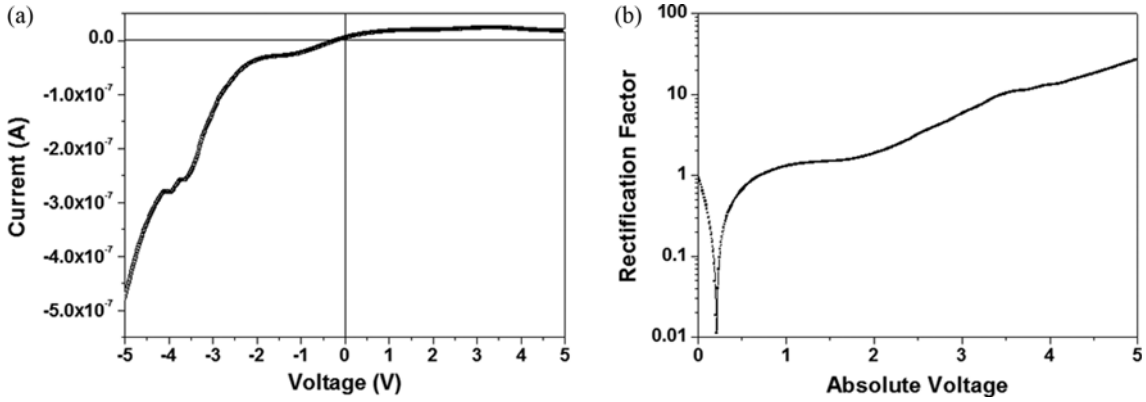

Fig. 6. (a) I-V curves of ZnO/Cu_2O structure and (b) rectification factor as a function of the applied bias.

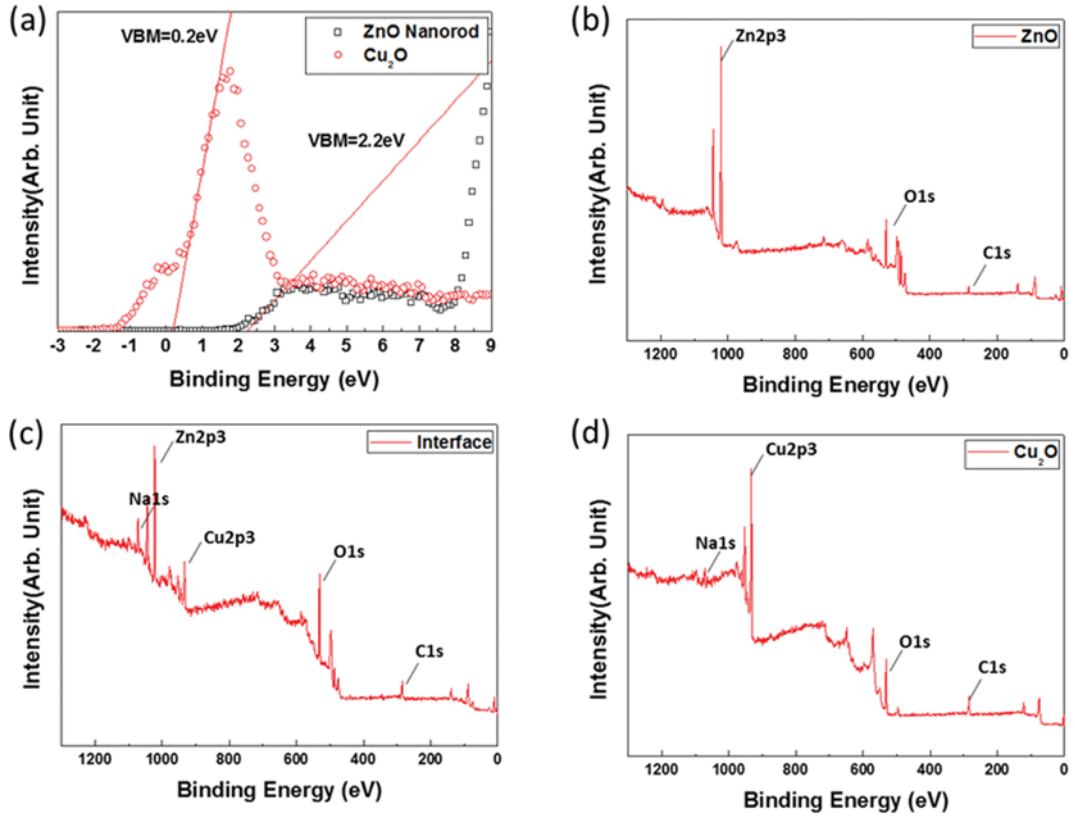

Fig. 8. XPS spectroscopy of (a) valance band edge spectra and (b), (c), (d) survey spectra of ZnO, ZnO/Cu_2O interface and Cu_2O, respectively.

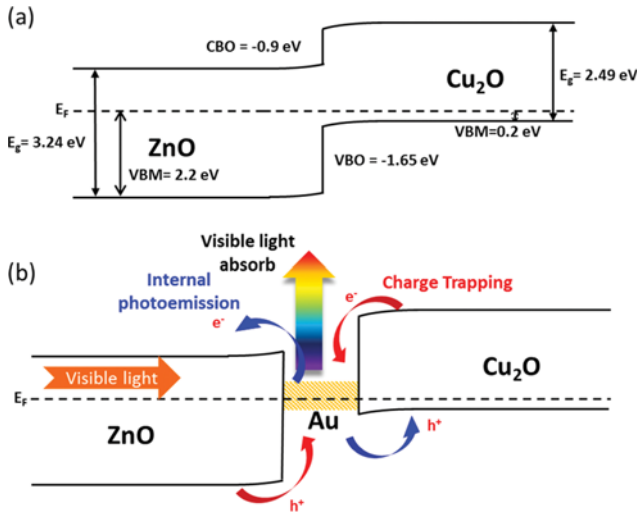

Fig. 9. Electronic band alignment of ZnO/Cu_2O heterostructure (a) without, and (b) with Au NP insertion, constructed by XPS and UV-Vis data.

Eqs. (1) and (2), respectively [35].

$$\Delta E_v = E^B_{VB} - E^A_{VB} + [(E^A_{CL} - E^{A/B}_{CL}) + (E^{B/A}_{CL} - E^B_{CL})] \quad (1)$$

$$\Delta E_C = E^B_g - E^A_g + \Delta E_V, \quad (2)$$

where E^A_{CL} and E^B_{CL} are the core-level energies of selected elements in the bulk material A and B; $E^{A/B}_{CL}$ and $E^{B/A}_{CL}$ are the core levels of A and B at the interface. In the present results, A and B are Cu_2O and ZnO nanorod, respectively. We estimated $(E^A_{CL} - E^{A/B}_{CL})$ as 0.19 eV and $(E^{B/A}_{CL} - E^B_{CL})$ as 0.16 eV. According to our results, the VBM energy positions relative to the Fermi energy level of ZnO nanorod and Cu_2O are −2.2 eV and −0.2 eV, respectively. In our experiments, valence band maximum was measured as 0.2 eV in binding energy in a reference to Fermi energy level (0 eV of binding energy). However, to use Kraut theory it should be the electron potential energy 'relative to the Fermi energy level', so it becomes −0.2 eV. Using this, VBO is calculated as −1.65 eV, while CBO is calculated as −0.9 eV [36-38]. Combining the acquired optical bandgap, VBO, CBO and VBM, a schematic band alignment model was proposed (Fig. 9). The band alignment showed highly p-type electrodeposited Cu_2O. The band bending at the interface showed cliff-like structures, which can increase recombination at the interface, reducing the open circuit voltage, V_{OC} [39-41]. Upon Au NP insertion, the band alignment suffers from a significant alteration due to the potential oxide/metal well-formation. This is due to the deep work function of Au>5 eV, which forms the double Schottky junctions with ZnO and Cu_2O. The Au-induced double junction leads to significant charge trap at the Au NP-induced potential well, which might hinder efficient charge separation across the heterojunction. This is a negative effect of Au NP insertion against the promotion of visible IPCE peak intensity and light absorption. In fact, absolute IPCE values for the stack with Au NP are lower than those without Au NP in the visible range, in spite of the max-

imum IPCE wavelength shift led by Au NP insertion. This should be overcome to maximize the absolute IPCE intensity by the plasmon hot carrier generation, which is indicated by carrier transport from Au to either ZnO (for electrons) or Cu_2O (for holes). This is equivalent to internal photoemission (IPE) [42] at a typical metal/semiconductor junction under the incident light exposure, with photon energy higher than the barrier height. Since the IPE yield is very low in the case of bulk heterojunction, the high generation rate and long lifetime of the Au NP-induced hot carrier generation can significantly increase carrier transport from Au to other oxides. This should be further studied to optimize the Au/oxide interface using various junction formation techniques. From the model shown in Fig. 9, since the ZnO/Au barrier height (>1 eV) is higher than the Au/Cu_2O barrier height (<0.3 eV), hot electron generation and transportation is more important, as it can be detrimental to the conversion efficiency.

CONCLUSIONS

ZnO nanorod/Au NP/Cu_2O heterojunction solar cells were fabricated, with solar cell characteristics being evaluated with respect to the LSPR effect. ZnO nanorod and Cu_2O layer structure were deposited using electrodeposition, while LSPR Au NPs were deposited using the E-beam evaporator. Size-controlled Au NPs showed a considerable change in absorbance in the visible light range. Improved light absorption was observed by Au NP insertion in the heterostructures. IPCE measurement under 1 sun condition showed that, by inserting size-tuned Au plasmon NPs with annealing in solar cells, peak IPCE wavelength can be adjusted to the visible light range. However, using optical bandgap and XPS-extracted VBM, VBO and CBO, band alignment suffers from significant alteration upon Au NP insertion, due to the potential oxide/metal well formation, which causes significant charge trap issues at Au NP-induced potential well, hindering efficient charge transport at the heterojunction. This should be overcome to maximize the absolute IPCE intensity by the plasmon hot carrier generation.

ACKNOWLEDGEMENTS

This work was supported by the Basic Science Research Program (NRF-2014R1A2A1A11053174) through the National Research Foundation of Korea (NRF) by the Ministry of Science, ICT, and Future Planning and the Ajou University research fund.

REFERENCES

1. P. V. Kamat, *J. Phys. Chem. C*, **111**, 2834 (2007).
2. J. J. Loferski, *J. Appl. Phys.*, **27**, 777 (1956).
3. C. Wadia, A. P. Alivisatos and D. M. Kammen, *Environ. Sci. Technol.*, **43**, 2072 (2009).
4. O. Ergen, A. Gibb, O. Vazquez-Mena, W. R. Regan and A. Zettl, *Appl. Phys. Lett.*, **106**, 103904 (2015).
5. A. Mittiga, E. Salza, F. Sarto, M. Tucci and R. Vasanthi, *Appl. Phys. Lett.*, **88**, 163502 (2006).
6. X. Chen, P. Lin, X. Yan, Z. Bai, H. Yuan, Y. Shen, Y. Liu, G. Zhang, Z. Zhang and Y. Zhang, *ACS Appl. Mater. Interf.*, **7**, 3216 (2015).
7. K. P. Musselman, A. Wisnet, D. C. Iza, H. C. Hesse, C. Scheu, J. L. MacManus-Driscoll and L. Schmidt-Mende, *Adv. Mater.*, **22**, E254 (2010).
8. F. Tsin, A. Venerosy, J. Vidal, S. Collin, J. Clatot, L. Lombez, M. Paire, S. Borensztajn, C. Broussillou and P. P. Grand, *Scientific Reports*, **5** (2015).
9. G. Gariné, E. Fernando, J. P. Carlos, E. M. Ricardo, M. Francisco, L. Dietmar, R. R.-B. José and A. D. Enrique, *J. Phys. D: Appl. Phys.*, **45**, 245301 (2012).
10. P. Mirtchev, K. Liao, E. Jaluague, Q. Qiao, Y. Tian, M. Varela, K. S. Burch, S. J. Pennycook, D. D. Perovic and G. Ozin, *J. Mater. Chem. A*, **2**, 8525 (2014).
11. B. D. Yuhas and P. Yang, *J. Am. Chem. Soc.*, **131**, 3756 (2009).
12. J. Luo, L. Steier, M.-K. Son, M. Schreier, M. T. Mayer and M. Grätzel, *Nano Lett.*, **16**, 1848 (2016).
13. Q. Liu, E. Sandgren, M. Barnhart, R. Zhu and G. Huang, *Photonics*, **2**, 893 (2015).
14. M. Abd-Ellah, J. P. Thomas, L. Zhang and K. T. Leung, *Solar Energy Mater. Solar Cells*, **152**, 87 (2016).
15. T. M. Mattox, X. Ye, K. Manthiram, P. J. Schuck, A. P. Alivisatos and J. J. Urban, *Adv. Mater.*, **27**, 5830 (2015).
16. S. Ren, B. Wang, H. Zhang, P. Ding and Q. Wang, *ACS Appl. Mater. Interfaces*, **7**, 4066 (2015).
17. M. Sriram, K. Zong, S. Vivekchand and J. J. Gooding, *Sensors*, **15**, 25774 (2015).
18. Y. Gao, F. Jin, Z. Su, H. Zhao, Y. Luo, B. Chu and W. Li, *Organic Electronics*, **39**, 71 (2016).
19. Y.-C. Yen, P.-H. Chen, J.-Z. Chen, J.-A. Chen and K.-J. Lin, *ACS Appl. Mater. Interfaces*, **7**, 1892 (2015).
20. S. Ahn, A. M. Nardes, D. Rourke, J. van de Lagemaat, N. Kopidakis and W. Park, Surface plasmon enhanced infrared absorption in p3ht-based organic solar cells: The effect of infrared sensitizer (presentation recording). In, 2015; 95620D-95620D-95621.
21. Y. Ievskaya, R. Hoye, A. Sadhanala, K. Musselman and J. MacManus-Driscoll, *Solar Energy Mater. Solar Cells*, **135**, 43 (2015).
22. M. Abdelfatah, J. Ledig, A. El-Shaer, A. Wagner, V. Marin-Borras, A. Sharafeev, et al., *Solar Energy Mater. Solar Cells*, **145**, Part 3, 454 (2016).
23. T. Shinagawa, M. Chigane, J. Tani and M. Izaki, Effect of oxide intermediate layers on pyramidally textured cu2o/zno solar cells prepared by electrodeposition. In:Meeting Abstracts: The Electrochemical Society, 2016; 1636-1636.
24. S. S. Jeong, A. Mittiga, E. Salza, A. Masci and S. Passerini, *Electrochim. Acta*, **53**, 2226 (2008).
25. J. Cui and U. J. Gibson, *J. Phys. Chem. C*, **114**, 6408 (2010).
26. K. P. Musselman, A. Marin, A. Wisnet, C. Scheu, J. L. MacManus-Driscoll and L. Schmidt-Mende, *Adv. Funct. Mater.*, **21**, 573 (2011).
27. D.-C. Perng, M.-H. Hong, K.-H. Chen and K.-H. Chen, *J. Alloys Compounds*, **695**, 549 (2017).
28. H. Dong, Z. Wu, A. El-Shafei, B. Xia, J. Xi, S. Ning, B. Jiao and X. Hou, *J. Mater. Chem. A*, **3**, 4659 (2015).
29. G. Q. Liu, Z. Q. Liu, Y. H. Chen, K. Huang, L. Li, F. L. Tang, L. X. Gong, Y. Hu and X. N. Zhang, *Optik - International Journal for Light and Electron Optics*, **124**, 5124 (2013).
30. Y. K. Lee, C. H. Jung, J. Park, H. Seo, G. A. Somorjai and J. Y. Park, *Nano Lett.*, **11**, 4251 (2011).

31. K. Jia, J.-L. Bijeon, P.-M. Adam and R. E. Ionescu, *Plasmonics*, **8**, 143 (2013).
32. Y. Nakano, S. Saeki and T. Morikawa, *Appl. Phys. Lett.*, **94**, 022111 (2009).
33. B. D. Viezbicke, S. Patel, B. E. Davis and D. P. Birnie, *Physica Status Solidi (b)*, **252**, 1700 (2015).
34. C. Honsberg and S. Bowden, ORG. (access April-June 2013) http://pveducation.org/pvcdrom/properties-of-sunlight/sun-position-calculator (2014).
35. E. A. Kraut, R. W. Grant, J. R. Waldrop and S. P. Kowalczyk, *Phys. Review B*, **28**, 1965 (1983).
36. K. Eom, S. Kim, D. Lee and H. Seo, *RSC Adv.*, **5**, 103803 (2015).
37. A. Santoni, F. Biccari, C. Malerba, M. Valentini, R. Chierchia and A. Mittiga, *J. Phys. D: Appl. Phys.*, **46**, 175101 (2013).
38. I.-H. Yoo, S. S. Kalanur, S. Y. Lee, K. Eom, H. Jeon and H. Seo, *RSC Adv.*, **6**, 82900 (2016).
39. C. Platzer-Björkman, C. Frisk, J. K. Larsen, T. Ericson, S.-Y. Li, J. J. S. Scragg, J. Keller, F. Larsson and T. Törndahl, *Appl. Phys. Lett.*, **107**, 243904 (2015).
40. X. Hao, K. Sun, C. Yan, F. Liu, J. Huang, A. Pu, et al., Large voc improvement and 9.2% efficient pure sulfide cu 2 znsns 4 solar cells by heterojunction interface engineering. In:Photovoltaic Specialists Conference (PVSC), 2016 IEEE 43rd: IEEE, 2016; 2164-2168.
41. X. Zheng, B. Chen, M. Yang, C. Wu, B. Orler, R. B. Moore, et al., *ACS Energy Lett.*, **1**, 424 (2016).
42. K. Yoon, J. K. Hyun, J. G. Connell, I. Amit, Y. Rosenwaks and L. J. Lauhon, *Nano Lett.*, **13**, 6183 (2013).